

Quantitative study of crossregulation, noise and synchronization between microRNA targets in single cells

Carla Bosia,^{1,*} Francesco Sgrò,^{2,*} Laura Conti,³ Carlo Baldassi,^{1,2} Federica Cavallo,³ Ferdinando Di Cunto,³ Emilia Turco,³ Andrea Pagnani,^{1,2,†} and Riccardo Zecchina^{1,2,†}

¹*Human Genetics Foundation, Torino, Italy*

²*Department of Applied Science and Technology, Politecnico di Torino, Italy*

³*Molecular Biotechnology Center, University of Torino, Italy*

(Dated: March 24, 2015)

Recent studies reported complex post-transcriptional interplay among targets of a common pool of microRNAs, a class of small non-coding downregulators of gene expression. Behaving as microRNA-sponges, distinct RNA species may compete for binding to microRNAs and coregulate each other in a dose-dependent manner. Although previous studies in cell populations showed competition in vitro, the detailed dynamical aspects of this process, most importantly in physiological conditions, remains unclear. We address this point by monitoring protein expression of two targets of a common miRNA with quantitative single-cell measurements. In agreement with a detailed stochastic model of molecular titration, we observed that: (i) crosstalk between targets is possible only in particular stoichiometric conditions, (ii) a trade-off on the number of microRNA regulatory elements may induce the coexistence of two distinct cell populations, (iii) strong inter-targets correlations can be observed. This phenomenology is compatible with a small amount of mRNA target molecules per cell of the order of $10 - 10^2$.

I. INTRODUCTION

Modern technologies to explore the transcriptome allow the identification of many non-coding transcripts whose functions are only partially known and that may control gene expression at different levels. MicroRNAs (miRNAs) are small post-transcriptional repressors of gene expression [1] belonging to this class of molecules. Known to play crucial roles in several biological processes, miRNAs often show altered expression profiles in human diseases [2–5]. It is commonly believed that miRNAs play central roles in conferring robustness to biological processes against environmental fluctuations [6–9]. The common assumption that one miRNA molecule can at one time at most interact with one target mRNA [10] suggests a whole new layer of post-transcriptional cross-regulation named the “Competing Endogenous RNA (ceRNA) effect” [11]. This theory proposes that the amount of a gene product may be tuned by varying the concentration of another gene sharing with it the same miRNAs. Qualitative experiments based on observing induced variations in transcripts indeed show that endogenous transcripts could be coupled due to the interaction with a common pool of miRNAs [12–15]. The discovery that miRNA-target interaction is compatible with a titration mechanism [16] supports the emergence of hypersensitivity regions [17, 18] where miRNA targets should be highly correlated and their relative stoichiometry tightly controlled [19, 20]. However, the relevance of the ceRNA effect is still largely debated: while absolute quantification experiments in primary hepatocytes and liver cells suggests that the ceRNA effect is unlikely to significantly affect gene expression and metabolism [21], differential susceptibility based on endogenous miRNA/target pool ratios provided a physiological context for ceRNA competition in vivo [22]. Crosstalk among mRNAs may thus be regulated depending on miRNA and mRNA relative abundances and may exhibit a complex phenomenology in terms of target correlation and relative fluctuation profiles [19].

Here, we experimentally explore these features addressing the relevance of the relative mRNA-miRNA stoichiometric composition. Through the design of two bidirectional plasmids, each with a two-color fluorescent reporter system, we simultaneously tracked gene expression in the presence and absence of miRNA regulatory elements (MRE). A stochastic gene interaction model [19] predicts the parameter region in which the targets are most correlated. Using flow cytometry measurements of cotransfected mammalian cells allowed us to quantify the crosstalk and correlations predicted by the model. We found that, besides the well-known “sponge effect” a given transfected target can exert on the others [23], there is an optimal range of parameters (in terms of effective transcription rates and miRNA interaction strengths) for which crosstalk is possible among ceRNAs. We show that such regulation arises both at the level of mean protein concentrations and noise and that it is compatible with low numbers of mRNA molecules. It is worth noting that an absolute quantification of exogenous transcripts reveals that in our experiments the crosstalk

* Joint First Authors

† Joint Last Authors

is highest in a *physiological* regime of order 10 to 10^2 molecules per cell [24, 25]. Moreover, there is a non-trivial competition mechanism on the number of available MRE such that synchronization can arise together with low noise. Interestingly, in agreement with the model, the same mechanism may induce bimodal population distributions with distinct high and low expression states of the targets.

II. STOCHASTIC TITRATION MODEL FOR CROSSTALK

We suggest a stochastic model for the miRNA-mediated target crosstalk that provides insight into target cross-regulation [16, 19, 26] (see Figure 1a). Through the formulation of a chemical master equation (see Material and Methods and Supplementary Information (SI) for details on the model), the model describes the amount of two free mRNAs r_1 and r_2 which are both targets of the same miRNA s , as a function of their constitutive expression r_0 (i.e. the value of r_1 or r_2 when g_1 or g_2 tend to 0). r_1 and r_2 can be translated into proteins (p_1 and p_2 respectively). The two candidate ceRNAs r_1 and r_2 , and thus p_1 and p_2 , are coupled through their common miRNA s which can bind both of them and then be released with or without degradation of r_1 or r_2 (miRNA turnover). The pool of available mature miRNAs is then the limiting factor in a system of potentially interacting targets. A Gaussian approximation of the master equation allows us to evaluate mean values and to quantify noise (coefficient of variation $CV_x = \sigma_{p_x}/p_x$) for p_1 , p_2 and p_0 (the protein translated from r_0) as well as the Pearson correlation coefficient between p_1 and p_2 (i.e. $(\langle p_1 p_2 \rangle - \langle p_1 \rangle \langle p_2 \rangle) / \sigma_{p_1} \sigma_{p_2}$), see Figures 1c-e respectively. Two parameters (g_1 and g_2) determine qualitatively the shapes of the functions generated by the model. These parameters are proportional to the miRNA-mRNA association rate. When one of them tends to zero (say g_2) then its corresponding target (r_2) is not interacting with the miRNA, while the other (r_1) behaves as described by Mukherji and coworkers [16]: as g_1 increases, r_1 (and then p_1) is repressed until a threshold level of r_0 is exceeded (Figure 1c). The threshold established by miRNA regulation and the increase of g_1 sharpens the transition between threshold and escape regimes. From the point of view of r_1 , g_2 (proportional to the association constant of the second target) governs the concentration of free miRNA available within the cell. Increasing g_2 (keeping all other parameters fixed) pushes the threshold to lower values of expression (lower r_0) and globally increases r_1 (and p_1): r_2 is behaving as a sponge for the miRNA, and increasing g_2 is equivalent to sponge away the miRNA available to target r_1 . When all the miRNA has been sponged away by r_2 (high value of g_2), then r_1 is not regulated anymore and its mean value is simply k_{r_1}/g_{r_1} (with k_{r_1} and g_{r_1} transcription and degradation rates of r_1 respectively). In an intermediate situation in which miRNA is not completely sponged away by one of the targets, finely-tuned crosstalk between targets is possible. The mathematical model thus suggests experiments to perform in order to test this hypothesis and to quantify the crosstalk, modulated by g_1 , g_2 and the amount of miRNA present in the cell.

III. FLOW CYTOMETRY REVEALS CROSS REGULATION

To investigate the predicted miRNA-mediated crosstalk in single mammalian cells, we used two different two-color fluorescent reporters, as sketched in Figure 1b. Both constructs consist of bidirectional promoters driving two genes whose products are fluorescent proteins. The first construct expresses the fluorescent proteins mCherry and enhanced yellow fluorescent protein (eYFP) [16], while the second construct expresses mCerulean and mKOrange. The 3'untranslated region (UTR) of both mCherry and mCerulean was engineered to contain a fixed number N of MRE for miR-20a (with $N = 0, 1, 4, 7$), a miRNA endogenously expressed by HEK 293 cell line [27, 28]. mCherry and mCerulean are therefore proxies for the two targets in the model. The 3'UTRs of eYFP and mKOrange were left unchanged in order to measure the transcriptional activity of the reporters in single cells. The constructs thus allow simultaneous monitoring of protein levels with (mCherry and mCerulean) and without (eYFP and mKOrange) miRNA regulation. In the case of single construct transfections, when individual cells are sorted according to their eYFP or mKOrange levels, we observed the threshold effect documented for HeLa cells by Mukherji and coworkers [16]. Briefly, when no MRE are present, mCherry (mCerulean) and eYFP (mKOrange) levels of expression are proportional. In cells with one or more miR-20a sites on mCherry (mCerulean), the mCherry (mCerulean) level does not increase until a threshold level of eYFP (mKOrange) is exceeded (see Figure 5). This indicates that the protein production is highly repressed below the threshold established by miRNA regulation and responds sensitively to target mRNA input close to it. Cotransfections of both constructs with different MRE numbers and measurements of fluorescence with flow cytometer enabled the quantification of crosstalk between mCherry and mCerulean as a function of N . We expect both mCherry and mCerulean signals to be proportional to p_1 and p_2 respectively, while eYFP (mKOrange) is proportional to p_0 . To quantitatively capture the crosstalk, we measured the joint distributions of mCherry (p_1) and eYFP (p_0) levels given mCerulean (p_2) in single cells positive to the fluorophores. We then binned the data according to their eYFP levels and calculated the mCherry and mCerulean mean levels as well as standard deviations in each

eYFP bin. Transient cotransfections allowed us to explore the space of parameters and manage $10^5 - 10^6$ cells. Our analysis has been restricted to cells whose fluorescence was 95% confidence above cellular autofluorescence and is independent of the transfection method.

IV. PHENOMENOLOGY OF CROSSTALK

To quantify the crosstalk by modulating g_1 and g_2 , we performed cotransfections with different MRE on mCherry and mCerulean ($N = 1, 4, 7$) and compared them with the case $N = 0$. We thus obtained 16 combinations of different cotransfections which allowed us to follow the expression of one target (mCherry) while tuning the amount of free miRNA via the second target (mCerulean). Our results are independent of the method of transfections as similar results were obtained by transfecting cells with lipofectamine-based (data reported in Figures 2-5,7,8) or CaCl_2 -based protocols (Figure 6). As predicted by the model (Figure 1c), it is possible to identify two different effects: (i) the appearance of a threshold on mCherry while increasing the number N of MRE on its 3'UTR and keeping $N = 0$ on mCerulean (Figure 2a and Figure 6a) and (ii) a global increase of mCherry mean fluorescence and a shift in the threshold while increasing N on mCerulean (Figure 2b and Figure 6b). mCherry thus tends to the unregulated case (mCherry linearly proportional to eYFP) while increasing the number of MRE on mCerulean. This result is well summarized by the fold repression F between regulated and unregulated mCherry mean fluorescence (Figure 2c-e). F is the ratio between the value of mCherry in the absence of miR-20a MRE and its value in the presence of MRE for each eYFP bin and for each N on mCerulean. Increasing the number of MRE on mCherry increases its repression, and F is highest when mCerulean has $N = 0$ MRE while tends to one increasing eYFP or the number of MRE on mCerulean. In particular, in proximity to the threshold, F shows a maximum whose value depends both on mCherry and mCerulean MRE. F could be indirectly considered as a measure of crosstalk between the two targets. Crosstalk is maximal for intermediate levels of repression, when mCerulean has between 1 and 4 MRE.

V. LOCAL INCREASE OF CELL-TO-CELL VARIABILITY: BIMODALITY

It is well known that the intrinsic noise of an unregulated gene product decreases when its expression level increases [29]. The effect of miRNA regulation could introduce an extra source of noise (extrinsic noise). Our mathematical model predicts that, at fixed levels of expression, the total noise (intrinsic plus extrinsic) of a miRNA-regulated gene product should increase upon enhancing miRNA-target interaction strength (see Figure 1d) with respect to the unregulated case. In particular the model predicts the onset of a local maximum in the noise profile of a miRNA target versus its level of constitutive expression for high miRNA-target interaction strength. Experimentally, we could identify two competing effects: (i) upon increasing N on mCherry (i.e. g_1) the total noise of mCherry, quantified by its CV, globally increases as a function of eYFP (Figure 3a and Figure 6c) and (ii) upon increasing N on mCerulean (i.e. g_2) the total noise of mCherry globally decreases (Figure 3b and Figure 6d). The overall result is that there is an optimal range of MRE on the ‘‘sponge’’ (mCerulean) for which a given miRNA-regulated target (mCherry) can show lower noise with respect to a target with lower N (compare Figures 3a and 3b). For high levels of repression (high N on mCherry and low N on mCerulean), mCherry CV eventually shows a local maximum in proximity to the threshold (Figure 6c,d). A low level of noise indicates unimodal distributions while an increase in noise stands for an increased cell-to-cell variability and may indicate bimodal population distributions with distinct high and low expression states [30]. We then checked if this was the case and found that bimodality on mCherry is present near the threshold in case of high miRNA-target interaction ($N = 4, 7$ on mCherry and $N = 0, 1$ on mCerulean), see histograms in Figure 3 and Figure 7. In particular, for $N = 7$ on mCherry and $N = 0$ on mCerulean two well discernible phenotypes appear. This suggests the binary response is directly linked to the variability in the level of repression the miRNA exerts on the target. The emergence of bimodality in the proximity of the miRNA-target threshold has been recently suggested [19].

VI. SHIFT OF THE OPTIMAL CROSSTALK REGION

In order to assess the crosstalk dependence on the availability of miRNA we transfected $100nM$ of pre-miR for miR-20a together with the bidirectional constructs. In our model this is equivalent to increasing the basal miRNA transcription rate k_s . We analyzed the cases with $N = 4$ for mCherry and $N = 0, 1, 4, 7$ for mCerulean. In agreement with the model predictions and with previous work [16], we observed a shift of the threshold towards higher eYFP levels (Figure 4a) together with a global increase in the fold-repression (Figure 4b) and a resulting shift of the optimal crosstalk region towards a higher number of MRE. We then quantified the absolute amount of exogenous targets in

three subpopulations of cells, sorted according to their eYFP intensity (low, medium and high) both in the presence and absence of pre-miR for the case with $N = 4$ on mCherry and $N = 1$ on mCerulean (Figure 4c). We found that mCherry and mCerulean ranged from 40 to 400 and from 10 to 250 molecules per cell, respectively, without pre-miR and both from 10 to about 100 molecules in the presence of pre-miR. In particular, the amount of exogenous targets for an intermediate level of eYFP is in quantitative agreement to what previously found [16]. These values show that even if the phenomenology so far described has been obtained through transient cotransfection, the numbers involved could be compatible with physiological values [22].

VII. POTENTIAL SYNCHRONIZATION IN PERMISSIVE ENVIRONMENT

Our model predicts a maximum in the correlation between two miRNA targets near the threshold (see Figure 1e). We investigated the strength of this prediction distinguishing between correlations dependent on the experimental setting (mainly transient cotransfections and partial sharing of regulatory elements in the promoter) and correlations induced by the competition for miRNA binding, which can potentially lead to synchronized fluctuations. We thus defined the ratio of the Pearson correlation coefficients (ratio of Pearson coefficient between mCherry and mCerulean possessing different MRE to the same measure in the absence of MRE). We measured this ratio for eYFP below, around and above the threshold (Figure 8a-c respectively), and observed that the competition for miRNA binding introduces correlations ranging from 4 to 12 fold higher than the basal level of correlation. Our results show that it is possible to have weakly or highly correlated targets for precise transcriptional programs. The regime of synchronized fluctuations is determined by the number of MRE on both the targets and by their relative stoichiometry.

VIII. DISCUSSION

Our results on miRNA-mediated target cross-regulation offer a detailed feature map to characterize the “ceRNA effect” (Figure 9). Besides the general consistency with previous population-based qualitative results [15], and the agreement with a titration-based mechanism of miRNA-target interaction [16, 19, 31], the stochastic analysis allowed us to characterize curve trends for fluctuations and correlations of two miRNA targets as function of their expression level. The detailed picture points out that crosstalk between targets is quantitatively relevant only in conditions of intermediate miRNA repression and small amounts of target molecules (order $10 - 10^2$), in agreement with a cell population-based study by Bosson and coworkers [22]. Since in this situation two or more targets may be highly cross-correlated, our result suggests that optimal levels of expression of genes and of miRNAs with respect to maximizing crosstalk may control relative fluctuations of targets that have to interact or bind in complexes with a precise stoichiometry [20]. On the other hand, we found that strong miRNA repression together with low target crosstalk is sufficient to induce bimodality, i.e. the appearance of two distinct population of cells with low and high target expression states. This result suggests that the system could be locked in one of these two states both changing the miRNA-target interaction strength through the expression of other competitors or through regulatory links. Such titrative regulatory mechanisms of miRNAs may easily switch ‘on’ or ‘off’ whole gene networks depending on miRNAs and targets relative stoichiometry. It is thus tempting to speculate that gene expression thresholding could be an important feature of cell fate decisions.

Although our experimental setting is “artificial”, i.e. induced by transient cotransfections of engineered plasmids, it provides a deep exploration of the parameter space. A physiological system of miRNAs and targets could indeed experience only a small subset of the features so far described, rendering the characterization of crosstalk difficult. The map of properties we ended up with (Figure 9) links quantitative measurements (effective miRNA repression and number of mRNA molecules) and model parameters (effective miRNA-target binding and transcription rates), suggesting the possibility to move around in phenotype space tuning quantities as the accessibility of binding sites or the affinity between miRNA and targets. In particular, it suggests the class of molecules we should look at when investigating for crosstalk. Molecular species physiologically present in the order of $10 - 10^2$ molecules per cell, such as transcription factors or signalling molecules [25, 32], are more likely to be affected by crossregulation since they are potentially closer to the threshold than highly expressed genes. We think that this findings would pave the way for significant progress in the understanding of pathological mechanisms underlying many diseases based on miRNA-target crosstalk dysregulation and therefore potentially lead to new therapeutic options. During the submission process of this paper we became aware of ref.[33] which contains results that partially overlap with a subset of ours.

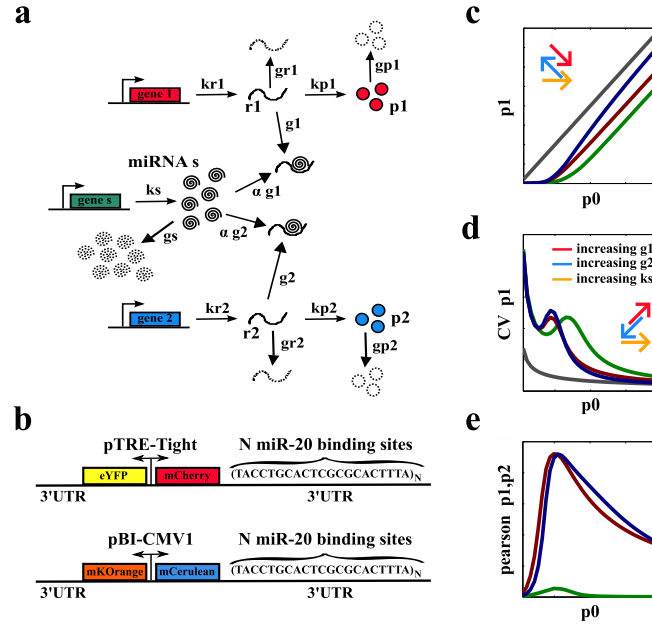


FIG. 1. **Model and predictions** (a) Sketch of the minimal model of miRNA-target interactions. One miRNA s and two targets r_1 and r_2 are independently transcribed with rates k_s , k_{r_1} and k_{r_2} , respectively. Each transcript can then degrade with rate g_s , g_{r_1} and g_{r_2} , respectively. Each miRNA s can interact with targets r_1 or r_2 with an effective binding rates g_1 or g_2 . α measures the probability of miRNA recycling. If not bound to a miRNA, targets r_1 and r_2 can be translated into proteins p_1 and p_2 respectively, which could then degrade with rates g_{p_1} and g_{p_2} . (b) Schematic representation of the two bidirectional plasmids coding for the four fluorophores. (c-e) Predictions from the stochastic model of interactions sketched in (a) in terms of mean amount of p_1 free molecules (c), p_1 coefficient of variation CV_{p_1} (d) and pearson correlation coefficient between p_1 and p_2 (e) as a function of p_0 , which is the constitutive value of p_1 when g_1 tends to 0. The colored arrows in (c) and (d) show the directions in which the curves move when tuning the miRNA-target interaction strengths g_1 and g_2 and the miRNA transcription rate k_s . Grey curves in (c,d) are predictions for p_1 and CV_{p_1} when g_1 tends to 0.

IX. MATERIALS AND METHODS

A detailed description of experimental procedures used in this study (including reporter plasmid construction, cell transfection, FACS measurement, cell sorting, qTR-PCR, modelling and data analysis procedures) is available in SI.

AUTHORS CONTRIBUTION

Carla Bosia (CB1), AP and RZ derived the stochastic model; CB1, FDC, ET, AP and RZ designed experiments; CB1, Carlo Baldassi (CB2) and AP analyzed data; CB1, FS, LC, FC and ET performed experiments; CB1, FS, LC, FDC, AP and RZ wrote the manuscript.

CORRESPONDING AUTHOR

Carla Bosia: carla.bosia@hugef-torino.org

ACKNOWLEDGMENTS

CB2 and RZ acknowledge the European Research Council for grant n. 267915. The authors would like to thank E. Fraenkel, A. Weisse and M. Osella for carefully reading the draft and U. Ala, F. Balzac, M. Caselle, P.P. Pandolfi, P. Provero, M. Osella and A. Riba for helpful discussions.

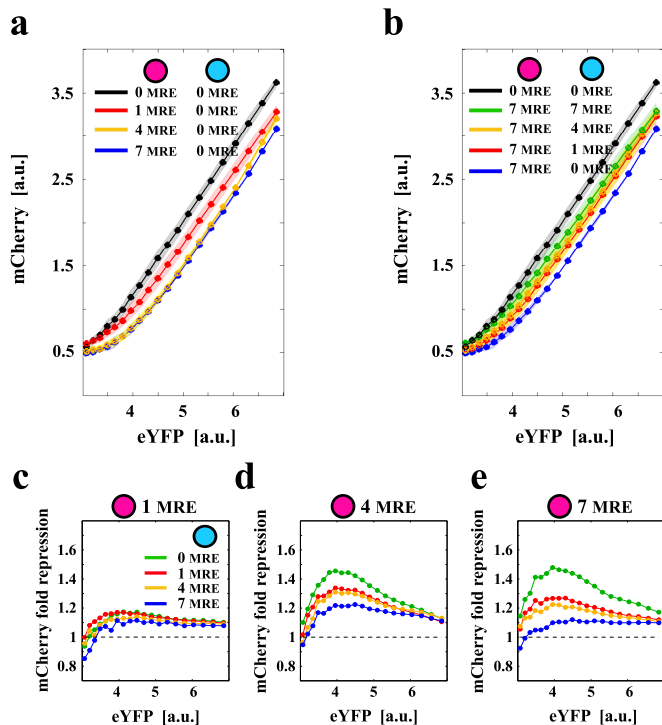


FIG. 2. **Threshold and fold-repression** (a-b) mCherry mean fluorescence is plotted against eYFP. Shaded strips around data are the error bars on the biological replicates. A threshold emerges when increasing mCherry MRE (a) while it disappears when increasing mCerulean MRE (b). The intensity of crosstalk (measured in terms of fold-repression F with respect to the unregulated fluorophores) depends on the particular combination of MRE on both exogenous targets (c-e). Purple and cyan circles in legends represent the plasmids coding for the mCherry and mCerulean fluorophores.

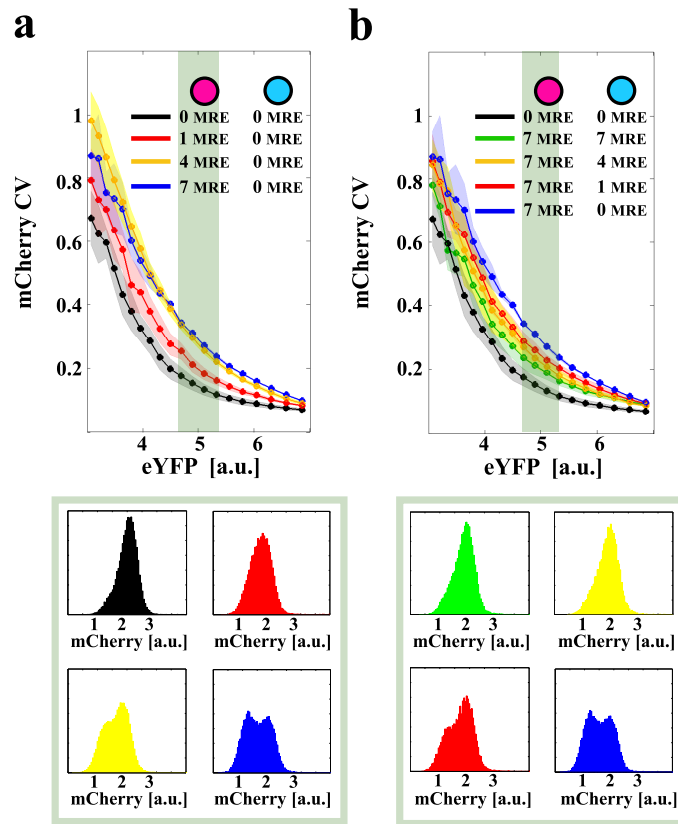


FIG. 3. **Local increase of cell-to-cell variability** (a-b) mCherry total noise quantified by its coefficient of variation (CV) is plotted against eYFP. Shaded strips around data are the error bars on the biological replicates. The CV globally increases when increasing the number of mCherry MRE (a) while decreases when increasing mCerulean MRE number (b). The competition of these two “strengths has the result of lowering the noise even if the expected repression from the rough number of mCherry MRE is high. Histograms in the lower panels show mCherry data distributions for the shaded regions in (a-b). A strong miRNA target repression strength increases cell-to-cell variability with the eventual appearance of different phenotypes (bimodal distributions). Purple and cyan circles in legends represent the plasmids coding for mCherry and mCerulean fluorophores, respectively.

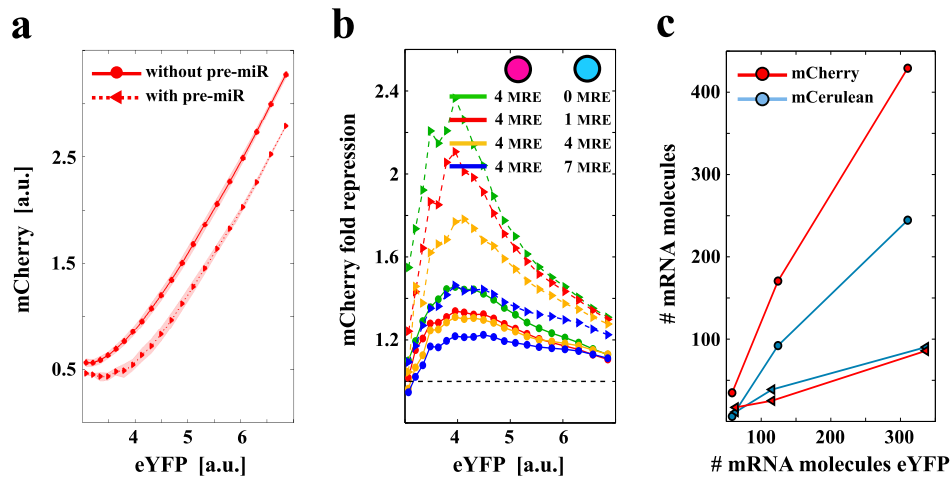


FIG. 4. **Shift of the optimal crosstalk region** (a) According to the model, increasing the pool of available miRNAs (transfecting pre-miRNAs) shifts the threshold to higher constitutive expression values. Shaded strips around data are the error bars on the biological replicates. (b) Different combinations of miR-20a MREs lead to different levels of fold repression and crosstalk. Purple and cyan circles in legends represent the plasmids coding for mCherry and mCerulean fluorophores, respectively. Triangles and circles in the plot are data from transfections with pre-miR20a and negative control respectively. (c) The mean amount of mRNA exogenous molecules per cell for three different intervals of eYFP basal expression is low enough to be comparable with physiological values. Triangles and circles show quantification in presence and absence of pre-miR-20a respectively.

SUPPLEMENTARY INFORMATION

A. Reporter plasmid construction

The set of fluorescent reporters coding for eYFP and mCherry was obtained from Addgene (#31463, #31464, #31465, #31466, deposited by Phil Sharp Lab) and are the same used in [16]. The second set of fluorescent reporters were cloned into pBI-CMV1 (Clontech). NLS sequence (ATGGGCCCTAAAAAGAAGCGTAAAGTC) was appended to mCerulean-N1 (Addgene #27795, deposited by Steven Vogel Lab [34]) by PCR and then inserted into the main vector with ClaI and BamHI. mKOrange-NLS (Addgene #37346, deposited by Connie Cepko Lab [35]) was cloned into the vector using EcoRI blunt and BamHI. miR-20a regulatory elements were appended to the 3'UTR of mCerulean with the same strategy applied in [16]

B. Transient transfections

We performed two different methods of transfection, with Lipofectamine (data in Figures 2-4 in the main text) and with CaCl₂ (data in Figures 1S-3S in SI). Lipofectamine transfection method: 293-HEK TeT-Off cells (Clontech) below passage 6 were plated in G418 (Gibco) 200 μ g/ml media in 6-well dishes the day before transfection. Reporter plasmids were transfected with Lipofectamine 2000 (Invitrogen) following the manufacturer's specifications. miR-20a pre and negative control (Ambion) were cotransfected at the indicated concentrations. Media was changed 24 h after transfection. Assays were performed 48 h after transfection. CaCl₂ transfection method: 293-HEK TeT-Off cells (Clontech) below passage 6 were plated in 100 \times 20 mm (Falcon BD) dishes the day before transfection. The cells were transfected using CaCl₂ protocols [36]. Media was changed 24 h after transfection. Assays were performed 48 h after transfection.

C. Flow cytometry

Cells were harvested 48 h after transfection (cell confluency \sim 90%) and run on a CyanADP (Beckman Coulter) flow cytometer. For each sample, at least $0.5 \cdot 10^6$ cells were acquired. The raw FACS data were analyzed with Summit3.1 software (Beckman Coulter) to gate cells according to their forward and side scatter profiles and to define the intensity of fluorescent signals emitted by the four reporters in each cell. These values were normalized for background fluorescence by subtracting the mean plus two standard deviation of the fluorescent signal measured in the untransfected control cells. Data were then binned according to their eYFP values.

D. Fluorescence-activated cell sorting

Cells were transfected with the $N = 4$ eYFP-mCherry and $N = 1$ mKOrange-mCerulean reporters and pre-miR-20a 100 nM (Ambion; PM10057) or Negative miRn20 100nM (Ambion). 48 h after transfection three cell populations were sorted according to their eYFP fluorescence value (low, medium and high YFP expression) using a BD FACS Aria III (Becton Dickinson) cell sorter. Cell pellets were washed and snap frozen before RNA isolation.

E. Quantitative Real-Time Polymerase Chain Reaction

Total RNA was extracted using Trizol reagent (Ambion Life Technologies, USA) in combination with Pure Link RNA Mini Kit (Ambion) from each sorted cell subpopulation. 1 μ g of total RNA was reverse transcribed using M-MLV reverse transcriptase and random primers (Life Technologies). Quantitative rt-PCR was performed on a 7300 Real Time PCR System (Applied Biosystems) using specific primers for eYFP, mCherry, mCerulean and mKOrange. 18S probe (Life Technologies) was used as internal control. Subsequent dilutions of each amplicon in known volumes allowed the definition of a calibration curve for each fluorophore directly linking threshold cycles and number of molecules per cell.

F. Empirical observables and Pearson correlation coefficient ratio

We defined the empirical average of a given observable O over an ensemble of cells with the symbol $\langle O \rangle = \sum_{i \in \text{cell}} O_i / N_{\text{cell}}$. The Pearson ratio is defined as the ratio of the Pearson correlation coefficient ($\rho_{x,y} = (\langle xy \rangle - \langle x \rangle \langle y \rangle) / \sigma_x \sigma_y$) between mCherry and mCerulean with a given combination of MRE to the same measure in absence of MRE. We evaluated the ratio for each eYFP bin (below, around and above threshold) for at least three different biological replicates. We then estimated the p-values of each ratio with respect to the distributions having as standard deviation the error on biological replicates and as mean values the Pearson ratio for mCherry and mCerulean with $N = 0$ MRE for the three eYFP intervals.

G. Stochastic model of molecular titration and crosstalk

1. Model definition

We describe with a stochastic model the miRNA-target interactions. The system can be described by 5 interacting variables (1 microRNA, 2 mRNAs, 2 proteins) indicated respectively as s, r_1, r_2, p_1, p_2 , which represent the (integer) copy number of molecules present in the cell at any given time t . Using this notation, the probability P of finding in a cell exactly s, r_1, r_2, p_1, p_2 molecules at any time t is governed by the following master equation:

$$\begin{aligned}
 \partial_t P = & \sum_{i=1}^2 [k_{r_i}(P_{r_i-1} - P) + k_{p_i} r_i (P_{p_i-1} - P)] + k_s (P_{s-1} - P) \\
 & + \sum_{i=1}^2 \{g_{r_i} [(r_i + 1)P_{r_i+1} - r_i P] + g_{p_i} [(p_i + 1)P_{p_i+1} - p_i P]\} + g_s [(s + 1)P_{s+1} - sP] \\
 & + a \sum_{i=1}^2 g_i [(r_i + 1)(s + 1)P_{r_i+1, s+1} - r_i s P] \\
 & + (1 - \alpha) \sum_{i=1}^2 g_i s [(r_i + 1)P_{r_i+1} - r_i P]
 \end{aligned} \tag{1}$$

where $P := P_{r_1, r_2, p_1, p_2, s}$ and, for example P_{p_2+1} is a short hand notation for $p_{r_1, r_2, p_1, p_2+1, s}$. In Eq. (1) k_{r_i}, k_s, k_{p_i} $i = 1, 2$, are the transcription rates of mRNAs r_i and microRNA s and the translation rates for proteins p_i respectively. g_{r_i}, g_{p_i}, g_s $i = 1, 2$ are their degradation rates. g_i $i = 1, 2$ are the effective association rates for the microRNA s and the mRNA r_i . Finally the parameter α measures the catalyticity of the interaction, *i.e.* the fraction of microRNA molecules that are recycled after the interaction with their targets. This master equation is not amenable for analytic solutions and approximate methods have been proposed [15, 19] to obtain accurate quantitative predictions. Following previous work [19] we obtained the approximated expression for mean values, standard deviations and Pearson correlation coefficients (sketched in Figure 1c-e), which we describe in the next paragraph.

2. Independent molecular-species approximation

As long as one is interested in mean values of the observables at steady state, a good approximation is the so-called independent molecular species approximation, also known as mean-field approximation which amounts to assume that the multivariate probability distribution P is factorized among the different chemical species:

$$P^{\text{ind}}(r_1, r_2, p_1, p_2, s) := p_{r_1}(r_1) p_{r_2}(r_2) p_{p_1}(p_1) p_{p_2}(p_2) p_s(s) . \tag{2}$$

Plugging this factorized functional form into Eq. (1), and computing the first moments at steady state (*i.e.* in the limit $t \rightarrow \infty$), one obtains a system of second order equations in the five variables which is easily solved numerically for any value of the model parameters. The main limitation of the factorized ansatz in Eq. (2) is that, although it empirically turns out to give a fairly accurate prediction of the mean values of the different chemical species across a wide range of parameters, the very simple structural form of Eq. (2) cannot predict their statistical correlations such as Pearson correlation coefficients which under the independent chemical species approximation are always zero by definition.

3. Gaussian Approximation

To overcome the above mentioned limitations and to take under control correlations across chemical species, a very simple yet accurate approximation scheme is the so-called Gaussian one [19]. Note that, following this approximation scheme copy numbers will not be bound to be integer numbers as it was the case in for the master equation defined in Eq. (1). As we will see in the following, and has already been extensively discussed in [19], this does not affect the good quality of the approximation. Let us denote with \vec{X} the five-dimensional vector of components r_1, r_2, p_1, p_2, s respectively. We can thus make the following multivariate Gaussian ansatz for the probability distribution function of \vec{X} :

$$P^{\text{Gauss}}(\vec{X}) := \frac{1}{\sqrt{(2\pi)^5 \det C}} \exp \left[-\frac{(\vec{X} - \vec{\mu})^T C (\vec{X} - \vec{\mu})}{2} \right], \quad (3)$$

which in our 5-dimensional case depends on 20 parameters: 5 numbers specify the mean $\vec{\mu}$ and 15 the covariance matrix C (which is symmetric). The key property that makes Eq. (1) very difficult to solve analytically is that, as shown in details in [19], it generates a whole hierarchy of moments such that the lower moments are expressed in terms of higher order moments and no moment-closure scheme can be utilized. Multivariate Gauss distributions, on the other hand, have the useful property that all moments can be expressed as a linear combination of just the first and the second moments. As an illustrative example, defining $\mu_i = E(X_i)$ and $E(X_i X_j) - E(X_i)E(X_j)$ for $i \neq j$, we could consider the generic third moment of the distribution defined in Eq. (3) $E(X_i, X_j, X_k) = C_{ij}\mu_k + C_{ik}\mu_j + C_{jk}\mu_i$ for $i \neq j \neq k$.

A systematic procedure to compute $\vec{\mu}$ and C requires to define the time dependent moment generating function:

$$F_t(\vec{z}) := \prod_{i=1}^5 z_i^{X_i} P_t(\vec{X}) \quad (4)$$

Plugging the above equation in the master equation we get the following second order partial differential equation:

$$\partial_t F_t(\vec{z}) = \mathcal{H}(\vec{z}) F_t(\vec{z}) \quad (5)$$

The moment generating function has the following properties:

$$\begin{aligned} F(\mathbf{z} = \mathbf{1}, \mathbf{q} = \mathbf{1}) &= 1, \\ \partial_{z_i} F|_{\mathbf{z}=\mathbf{1}, \mathbf{q}=\mathbf{1}} &= \langle X_i \rangle, \\ \partial_{z_i}^2 F|_{\mathbf{z}=\mathbf{1}, \mathbf{q}=\mathbf{1}} &= \langle X_i^2 \rangle - \langle X_i \rangle^2, \\ \partial_{z_i, z_j}^2 F|_{\mathbf{z}=\mathbf{1}, \mathbf{q}=\mathbf{1}} &= \langle X_i X_j \rangle. \end{aligned} \quad (6)$$

By inserting the previous definitions and imposing the Gaussian marginalization conditions mentioned above, we obtain a system of 20 equations in 20 unknown that we can numerically solve to get the values for $\vec{\mu}$ and C . As already shown in [19], this approximation turns out to reproduce fairly accurately both noise (in terms of coefficient of variation CV) of single targets and Pearson correlation coefficient between targets, when compared with the numerical values obtained through Gillespie algorithm.

SUPPLEMENTARY FIGURES

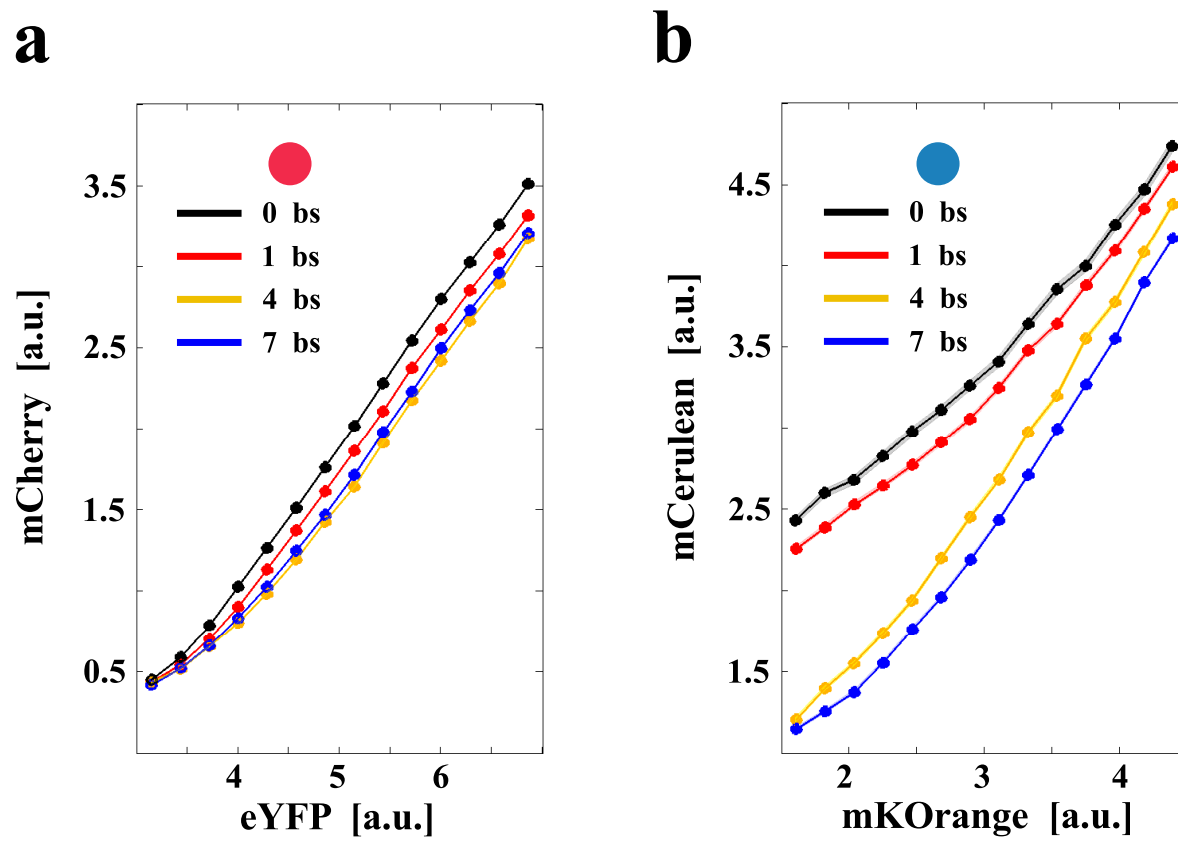


FIG. 5. **Threshold for single plasmid transfections with CaCl_2** (a) mCherry mean fluorescence is plotted against eYFP. A threshold emerges when increasing mCherry bs. The same holds for mCerulean with respect to mKOrange (b). Shaded strips around data are the error bars on the biological replicates. Red and cyan circles in legends represent the mCherry and mCerulean fluorophores.

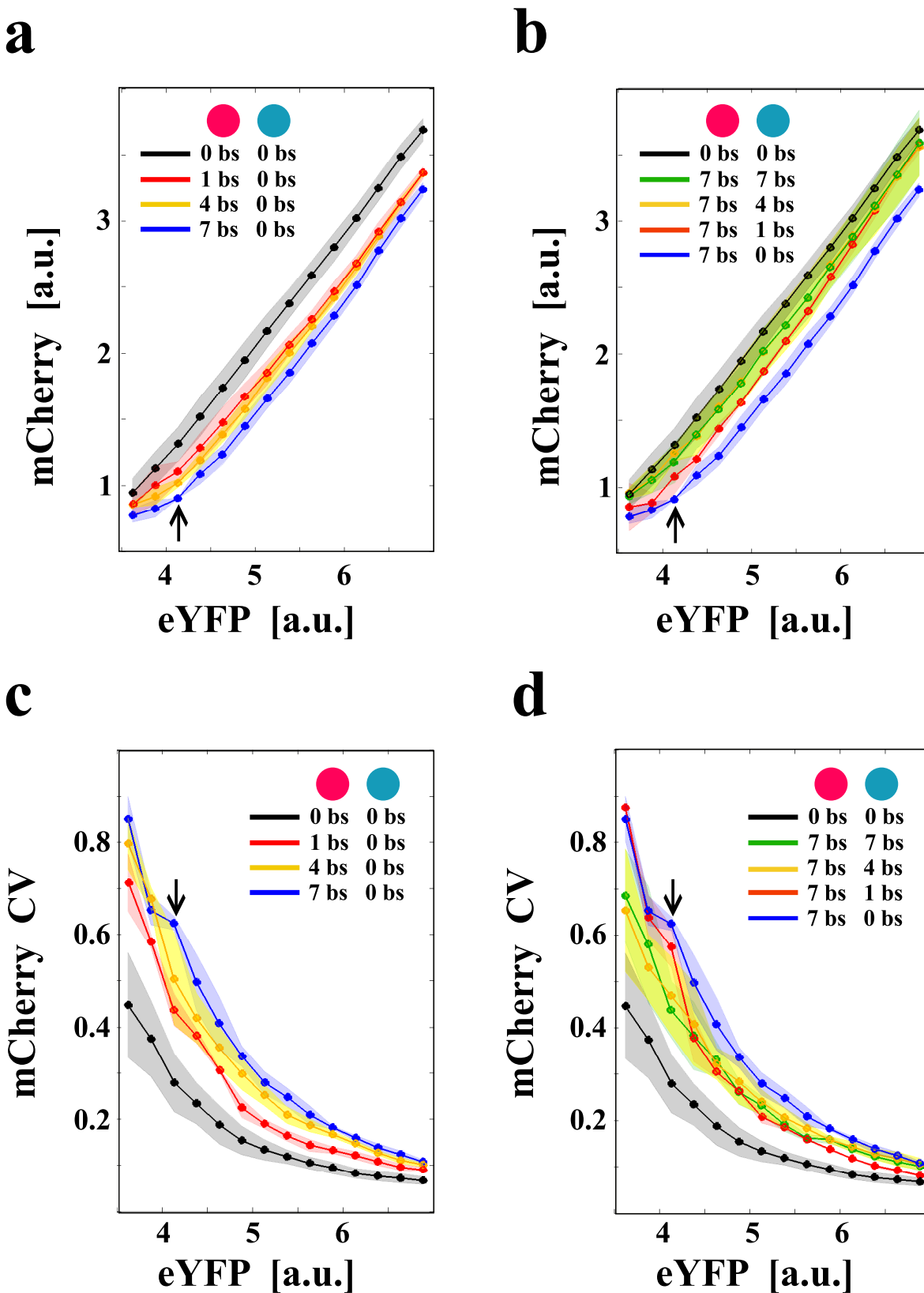


FIG. 6. **Threshold and noise for CaCl_2 transfections** (a-b) mCherry mean fluorescence is plotted against eYFP. Shaded strips around data are the error bars on the biological replicates. A threshold emerges when increasing mCherry MREs (a) while it disappears when increasing mCerulean MREs (b). (c-d) mCherry coefficient of variation (CV) is plotted against eYFP. Shaded strips around data are the error bars on the biological replicates. The CV of mCherry globally increases when increasing mCherry MREs (a) while decreases when increasing mCerulean MREs (b). Red and cyan circles in legends represent the mCherry and mCerulean fluorophores. Black arrows point to the threshold.

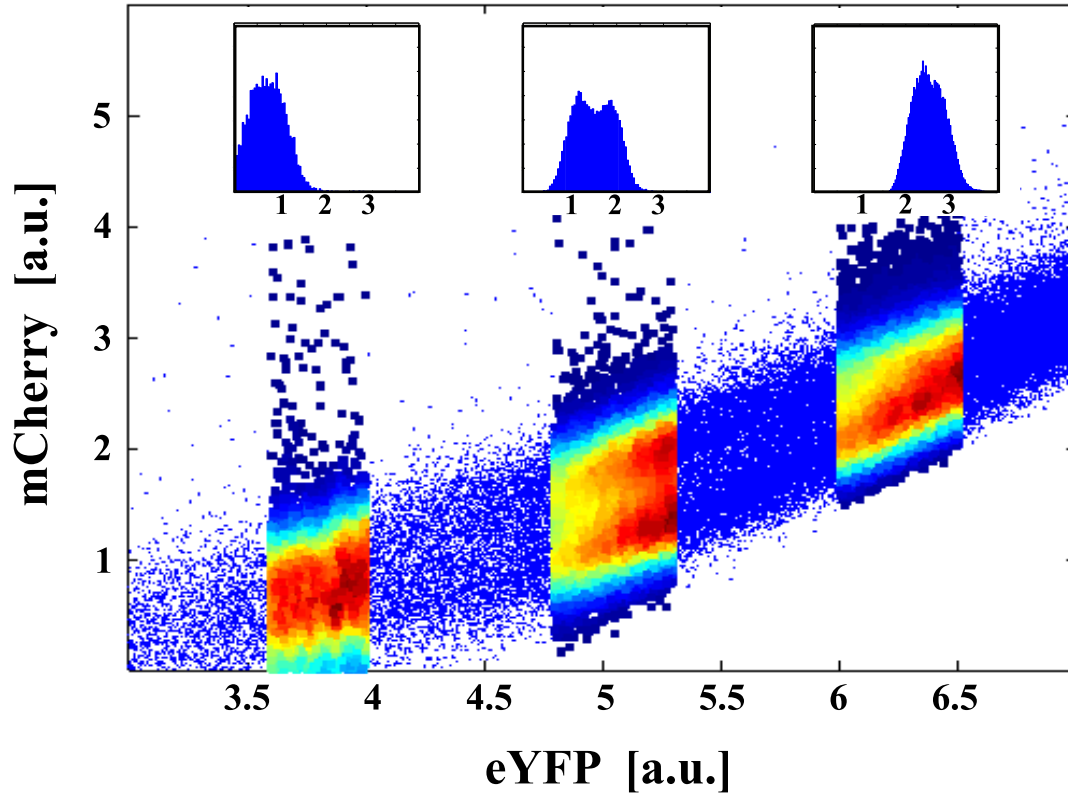


FIG. 7. **Strong miRNA-target interaction engenders bimodality** Rough mCherry cytofluorimetry data scattered against eYFP. Soon after the threshold two clear phenotypes appear.

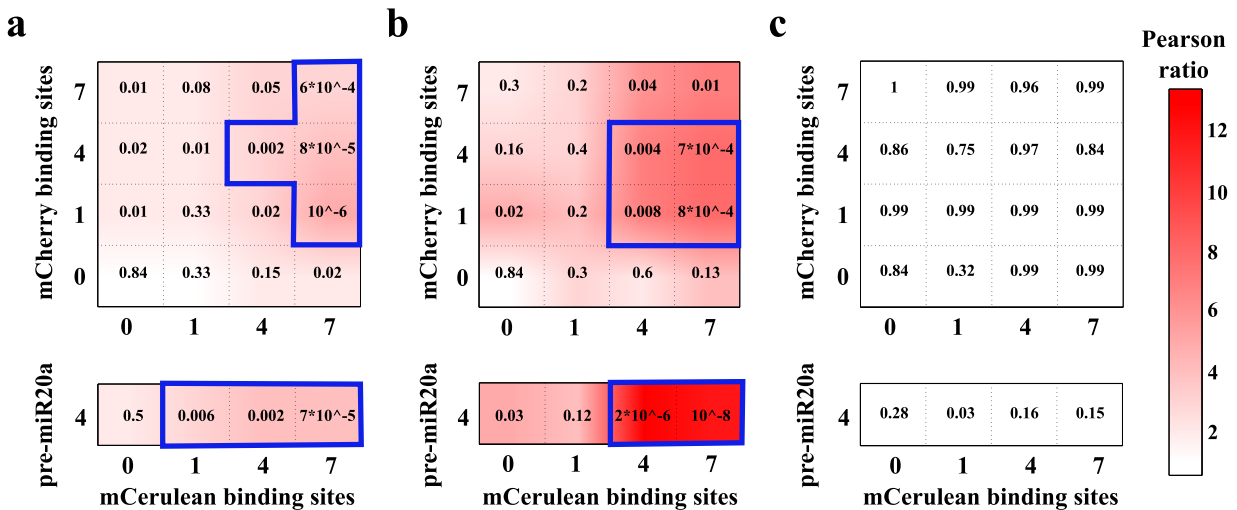


FIG. 8. **Fold Pearson and p-values** The Pearson ratio is measured for three different values of eYFP basal expression: below threshold (a), around threshold (b) and above threshold (c). p-values are reported for each combinations of miRNA MREs on the two plasmids. The regions inside the blue perimeters are those statistically significant with p-values < 0.01 . As predicted by the model, the correlation is maximal around the threshold and could be even 12 fold higher than in the unregulated case. Blue-delimited areas are regions whose Pearson ratio (i.e. ratio of Pearson coefficient between mCherry and mCerulean possessing different MRE to the same measure in the absence of MRE) is statistically relevant with respect to the corresponding unregulated case.

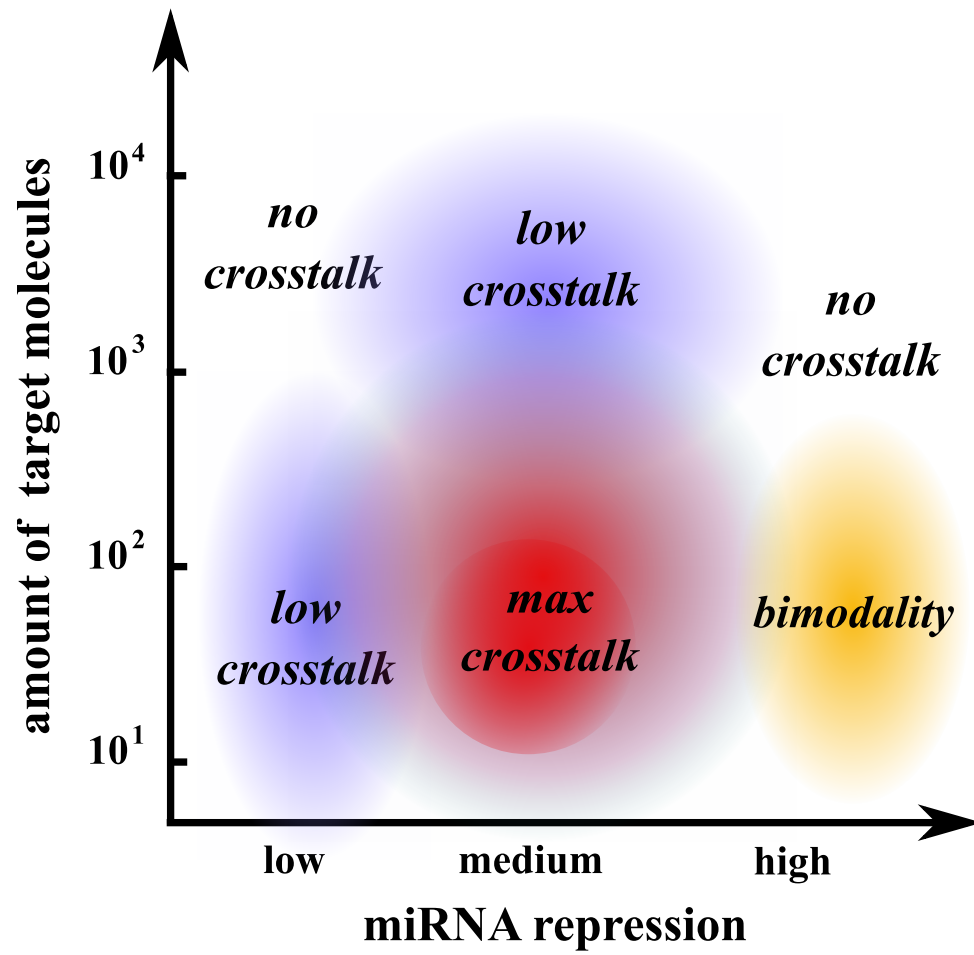


FIG. 9. **Map of phenomenology** The cartoon shows how the crosstalk between targets and bimodality on mCherry behave varying effective miRNA repression strength and target molecule amounts.

-
- [1] Alex S Flynt and Eric C Lai. Biological principles of microRNA-mediated regulation: shared themes amid diversity. *Nat Rev Genet*, 9(11):831–842, Nov 2008.
 - [2] David P Bartel. MicroRNAs: genomics, biogenesis, mechanism, and function. *Cell*, 116(2):281–297, Jan 2004.
 - [3] Natascha Bushati and Stephen M Cohen. microRNA functions. *Annu Rev Cell Dev Biol*, 23:175–205, 2007.
 - [4] Ines Alvarez-Garcia and Eric A Miska. MicroRNA functions in animal development and human disease. *Development*, 132(21):4653–4662, Nov 2005.
 - [5] Aurora Esquela-Kerscher and Frank J Slack. Oncomirs - microRNAs with a role in cancer. *Nat Rev Cancer*, 6(4):259–269, Apr 2006.
 - [6] Xin Li, Justin J. Cassidy, Catherine A. Reinke, Stephen Fischboeck, and Richard W. Carthew. A microRNA imparts robustness against environmental fluctuation during development. *Cell*, 137(2):273–282, Apr 2009.
 - [7] Masafumi Inui, Graziano Martello, and Stefano Piccolo. MicroRNA control of signal transduction. *Nat Rev Mol Cell Biol*, 11(4):252–263, Apr 2010.
 - [8] M Osella, C Bosia, D Corá, and M Caselle. The role of incoherent microrna-mediated feedforward loops in noise buffering. *PLoS Comput Biol*, 7(3):e1001101, 2011.
 - [9] Carla Bosia, Matteo Osella, Mariama El Baroudi, Davide Corá, and Michele Caselle. Gene autoregulation via intronic micrnas and its functions. *BMC Systems Biology*, 6:131, 2012.
 - [10] Aaron Arvey, Erik Larsson, Chris Sander, Christina S Leslie, and Debora S Marks. Target mrna abundance dilutes microrna and sirna activity. *Molecular Systems Biology*, 6(1), 2010.
 - [11] L Salmena, L Poliseno, Y Tay, L Kats, and PP Pandolfi. A cerna hypothesis: the rosetta stone of a hidden rna language? *Cell*, 146(3):353–358, 2011.
 - [12] P. Sumazin, X. Yang, and H.-S. et al. Chiu. An extensive microrna-mediated network of rna-rna interactions regulates established oncogenic pathways in glioblastoma. *Cell*, 147(2):370–381, 2011.
 - [13] Y. Tay, L. Kats, and L et al. Salmena. Coding-independent regulation of the tumor suppressor pten by competing endogenous mrnas. *Cell*, 147(2):344–357, 2011.
 - [14] F. Karreth, Y. Tay, and D. et al. Perna. In vivo identification of tumor- suppressive pten cernas in an oncogenic braf-induced mouse model of melanoma. *Cell*, 147(2):382–395, 2011.
 - [15] U Ala, FA Karreth, C Bosia, A Pagnani, R Taulli, V Léopold, Y Tay, P Provero, R Zecchina, and PP Pandolfi. Integrated transcriptional and competitive endogenous rna networks are cross-regulated in permissive molecular environments. *Proc Natl Acad Sci U S A*, 110(18):7154–7159, 2013.
 - [16] S Mukherji, MS Ebert, GX Zheng, JS Tsang, PA Sharp, and A van Oudenaarden. Micrnas can generate thresholds in target gene expression. *Nat Genet*, 43(9):854–859, 2011.
 - [17] J Elf, J Paulsson, O Berg, and M Ehrenberg. Near-critical phenomena in intracellular metabolite pools. *Biophysical Journal*, 84:154–170, 2003.
 - [18] N Buchler and M Louis. Molecular titration and ultrasensitivity in regulatory networks. *Journal of Molecular Biology*, 384:1106–1119, 2008.
 - [19] Carla Bosia, Andrea Pagnani, and Riccardo Zecchina. Modelling competing endogenous rna networks. *PLoS One*, 8(6):e66609, 2013.
 - [20] A Riba, C Bosia, M El Baroudi, L Ollino, and M Caselle. A combination of transcriptional and microrna regulation improves the stability of the relative concentrations of target genes. *PLoS Comput Biol*, 10(2):e1003490, 2014.
 - [21] R. Denzler, V. Agarwal, J. Stefano, D. P. Bartel, and M. Stoffel. Assessing the cerna hypothesis with quantitative measurements of mirna and target abundance. *Molecular Cell*, 54(5):766–776, 2014.
 - [22] A. D. Bosson, J. R. Zamudio, and P. A. Sharp. Endogenous mirna and target concentrations determine susceptibility to potential cerna competition. *Molecular Cell*, 56:347–359, 2014.
 - [23] MS Ebert and PA Sharp. Microrna sponges: progress and possibilities. *RNA*, 16:2043–2050, 2010.
 - [24] B Schwanhäusser, D Busse, N Li, G Dittmar, J Schuchhardt, J Wolf, W Chen, and M Selbach. Global quantification of mammalian gene expression control. *Nature*, 473:337–342, 2011.
 - [25] G.K. Marinov, B.A. Williams, K. McCue, G.P. Schroth, J. Gertz, R.M. Myers, and B.J. Wold. From single-cell to cell-pool transcriptomes: Stochasticity in gene expression and rna splicing. *Genome Research*, 24:496–510, 2014.
 - [26] Erel Levine, Zhongge Zhang, Thomas Kuhlman, and Terence Hwa. Quantitative characteristics of gene regulation by small RNA. *PLoS Biol*, 5(9):e229, Sep 2007.
 - [27] C. Mayr and D.P. Bartel. Widespread shortening of 3’utrs by alternative cleavage and polyadenylation activates oncogenes in cancer cells. *Cell*, 138:673–684, 2009.
 - [28] S Rügger and Grosshans H. Microrna turnover: when, how, and why. *Trends in Biochemical Sciences*, 37: 10:436–446, 2012.
 - [29] M. Krn, T.C Elston, W.J. Blake, and J.J. Collins. Stochasticity in gene expression: from theories to phenotypes. *Nature Reviews Genetics*, 6:451–464, 2005.
 - [30] W. Blake, M. Kaern, C.R. Cantor, and J.J. Collins. Noise in eukaryotic gene expression. *Nature*, 422:633–637, 2003.
 - [31] M. Figliuzzi, E. Marinari, and A. De Martino. Micrnas as a selective channel of communication between competing rnas: a steady-state theory. *Biophysical Journal*, 104(5):1203–1213, 2013.
 - [32] G Li, D Burkhardt, C Gross, and JS Weissman. Quantifying absolute protein synthesis rates reveals principles underlying allocation of cellular resources. *Cell*, 157:624–635, 2014.

- [33] Ye Yuan, Bing Liu, Peng Xie, Michael Q. Zhang, Yanda Li, Zhen Xie, and Xiaowo Wang. Model-guided quantitative analysis of microRNA-mediated regulation on competing endogenous RNAs using a synthetic gene circuit. *Proceedings of the National Academy of Sciences*, 112(10):3158–3163, 2015.
- [34] S.V. Koushik, H. Chen, C. Thaler, H.L. Puhl, and S.S. Vogel. Cerulean, venus, and venusy67c fret reference standards. *Biophysical Journal*, 91(12):L99–L101, 2006.
- [35] K.T. Beier, M.E. Samson, T. Matsuda, and C.L. Cepko. Conditional expression of the *tva* receptor allows clonal analysis of descendants from cre-expressing progenitor cells. *Developmental Biology*, 353(2):309–20, 2011.
- [36] M. Jordan, A. Schallhorn, and F.M. Wurm. Transfecting mammalian cells: optimization of critical parameters affecting calcium-phosphate precipitate formation. *Nucleic Acids Research*, 24(4):596–601, 1996.